INITIAL ESTIMATES OF RADIATION BACKGROUNDS
FOR THE HARD X-RAY TELESCOPE (HXT)
ON THE PLANNED CONSTELLATION-X MISSION

T. W. Armstrong[1], B. L. Colborn[1], and B. D. Ramsey[2]

[1]Science Applications International Corp.(SAIC), 1706 Prospect Rd., Prospect, TN 38477
[2]NASA Marshall Space Flight Center, Huntsville, AL 35812

ABSTRACT – Monte Carlo simulations have been made to predict radiation backgrounds for the HXT CdZnTe x-ray detector, a candidate imaging spectrometer for deployment on the planned Constellation-X mission. The x-ray spectrum in the 5-100 keV range has been calculated for: the prompt background due to GCR proton interactions in the detector assembly and spacecraft, the delayed background due to decay emissions from material activation, and the diffuse cosmic x-ray background. The calculations are made for a baseline Constellation-X orbit at Libration Point L2. For comparison, estimates have also been made for a low Earth orbit deployment where background effects from the trapped proton belt are also included. Based on these simulation results, suggestions are made for design modifications to the detector shield that may substantially reduce the background levels.

CONTENTS

1. INTRODUCTION

As a next-generation, space-based x-ray observatory, the Constellation-X mission consisting of multiple spacecraft, to obtain a large collecting area, and a Libration Point (L2) orbit, to optimize viewing time, has been proposed [1]. One of the planned instruments is a hard x-ray telescope (HXT) with focusing optics and Cadmium-Zinc-Telluride (CZT) detectors for high resolution measurements in the 5 - 40 keV, or perhaps higher, energy range. The purpose here is to present results from simulations that have been made to estimate the HXT background induced by the ambient space radiation environment.

The baseline orbit for the Constellation-X mission is a stationary Libration Point orbit at position L2, located about 1.5×10^6 km from the Earth, so the ambient radiation environments of concern for inducing HXT backgrounds are galactic cosmic rays (GCR) and diffuse cosmic x-rays. In addition to this baseline, we have also made for comparison background estimates for deployment in a low Earth orbit (LEO) using a circular orbit at 500 km altitude and 28.5° inclination as an example. For the LEO orbit, background production from the geomagnetically trapped protons is also included.

For these initial HXT background estimates, several simplifying assumptions have been made. In particular, the detector assembly used in the simulations is based on a preliminary conceptual design and simple computational model. While a detector assembly configuration including an active shield with anti-coincidence counting has been modeled, it has not yet been optimized for background reduction. A very simplified mass model of all other instruments and the spacecraft, consisting of a single cylinder of reduced density aluminum, has been used. Also, some simplifying assumptions in the calculational procedure have been made, as discussed in Sec. 3, which, although reasonable for these scoping estimates, need to be removed for more accurate estimates as the HXT design evolves.

2. SIMULATION METHODS

2.1 Configuration Model

The simple detector assembly model illustrated in Fig. 1, based on information provided by Caltech and NASA/GSFC [2], was used for the background simulations. The CZT detector

Dimensions:

• Passive Collimator
    120 cm height
    2.51 cm inner radius
    thin-wall, high-Z material

• BGO Shield
    31 cm height
    2.51 cm inner radius
    1.90 cm wall thickness

• CZT Detector
    0.10 cm thickness
    1.43 cm radius
    4.0 cm from bottom of well

• Electronics (Si)
    1.43 cm radius
    0.50 mm thickness

• Spacecraft
    85 cm height
    110 cm radius
    750 kg

Passive Collimator

BGO Active Shield
& Collimator

CZT Detector

Electronics

Spacecraft

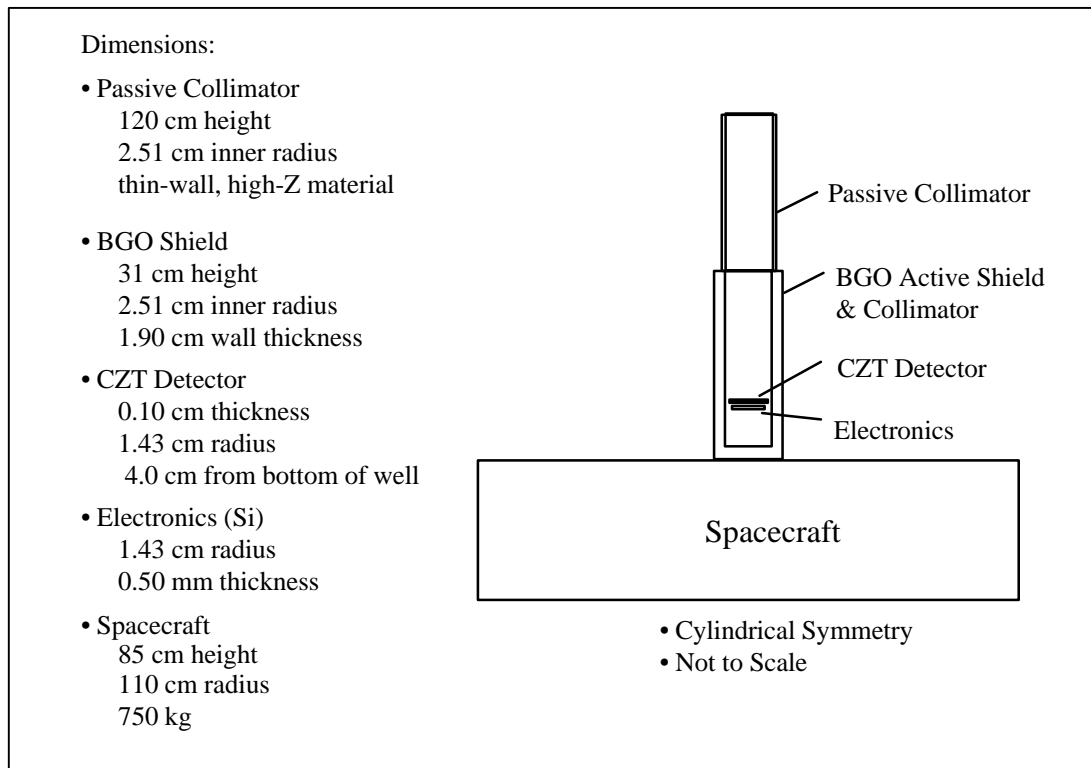• Cylindrical Symmetry
• Not to Scale

Fig. 1. HXT detector assembly and spacecraft model used for background simulations.

(1 mm thick, 1.43 cm radius) is located in a well-type BGO active shield. The top of the BGO cylinder is 25 cm above the detector, so the BGO serves as a collimator also. The wall and bottom of the BGO are relatively thick, 1.90 cm, corresponding to an areal density of 13.5 g/cm^2. A thin (0.5 mm) layer of silicon was placed below the detector to represent electronics.

A passive collimator 120 cm long is included above the BGO to further reduce the diffuse background. This length was selected for these initial estimates so that the diffuse background would not be significant relative to other background sources for energies above roughly 10 keV. (As shown later, the magnitudes of the other background sources are such that a somewhat longer passive collimator would be desirable so that the diffuse background would not be significant above the minimum measurement energy of about 5 keV, and, based on preliminary designs of the detector assembly layout on the spacecraft [3], a longer passive collimator is feasible.) Since the collimator need only attenuate the low-energy diffuse background, it can be constructed as a thin wall of high-Z material, resulting in relatively low mass and activation. The wall area viewed by the detector is so small that the collimator is not

expected to be a significant activation source, and passive collimator activation as a background source has been ignored here. The total (BGO plus passive) collimator length of 145 cm, gives a detector solid angle of 9.37 x 10^{-4} steradians and a full-width field-of-view of 2.0 deg.

The cylindrical detector assembly is placed above the center of a cylindrical volume representing the spacecraft bus and other components. The dimensions of the bus are based on information provided by NASA/GSFC [3] corresponding to a six spacecraft constellation being considered. The spacecraft mass used (750 kg) includes the bus mass (610 kg) plus 140 kg for a microcalorimeter detector array with cryostat expected to be onboard.

The material compositions used are summarized in Table 1. As indicated, the spacecraft was modeled as a homogeneous volume of reduced-density aluminum.

Table 1. Materials and compositions used.

Component	Material	Composition	Density (g/cm^3)	Fill Factor	Density Used (g/cm^3)
Spacecraft	Homog Al	Al	2.7	0.0926	0.25
Electronics	Si	Si	2.3	1.0	2.3
Shield/Collimator	BGO	$Bi_4Ge_3O_{12}$	7.13	1.0	7.13
Detector	CZT	$Cd_{0.9}Zn_{0.1}Te$	6.00	1.0	6.00

2.2 Ambient Radiation Environment

For the L2 orbit background calculations, a model fit [4] to 1986 solar minimum measurements was used for the ambient galactic cosmic-ray spectrum, as shown in Fig. 2. For the diffuse cosmic x-ray background flux, the following fit to data by Schwartz as quoted in [5] was used: $\phi_x(E) = 8.5\,E^{-1.40}$ for $1 < E < 21$ keV and $\phi_x(E) = 167\,E^{-2.38}$ for $E \geq 21$ keV, where the flux units are photons/cm^2 - s - keV - sr.

For the LEO background calculations, the orbit average GCR proton spectrum was obtained by using the exomagnetospheric spectrum for L2 and applying an orbit-average, rigidity-dependent geomagnetic transmission function calculated using the CREME96 code [6].
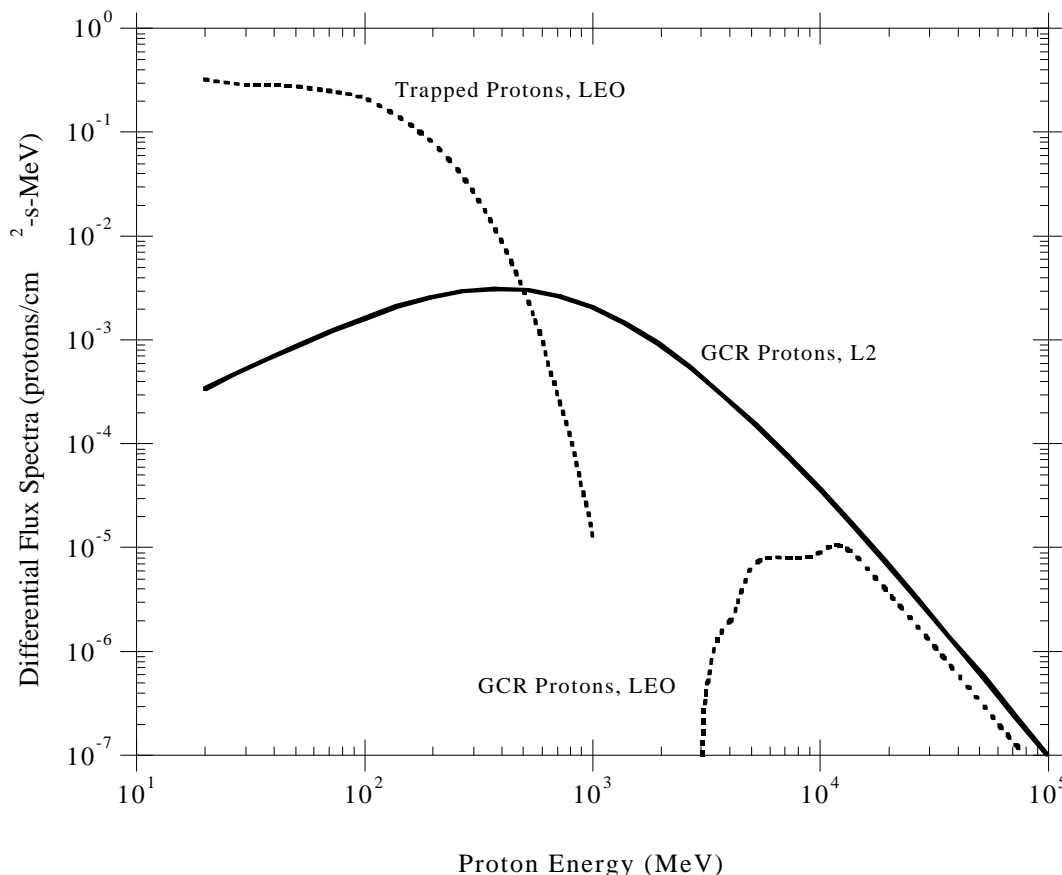
Fig. 2. Ambient proton background spectra for a libration point (L2) orbit and an example
low Earth orbit (LEO) at 500 km. altitude and 28.5 deg. inclination.

The LEO trapped proton spectrum was predicted using the AP8 trapped proton model [7] at solar minimum and the TRAP/SEE code [8].

2.3 Radiation Transport

The prompt GCR-induced background predictions have been made using the coupled Monte Carlo code system shown in Fig. 3, which accounts for hadronic, electromagnetic, and low-energy neutron transport. This methodology has been applied at SAIC to predict radiation backgrounds for numerous space-borne detector systems, including x-ray detectors for the AXAF and INTEGRAL missions [9,10].

Input Data	Data Prep. Codes	Radiation Transport Codes	Analysis Codes	Output

Fig. 3. Coupled set of Monte Carlo radiation transport codes used for predicting prompt detector background from GCR protons.

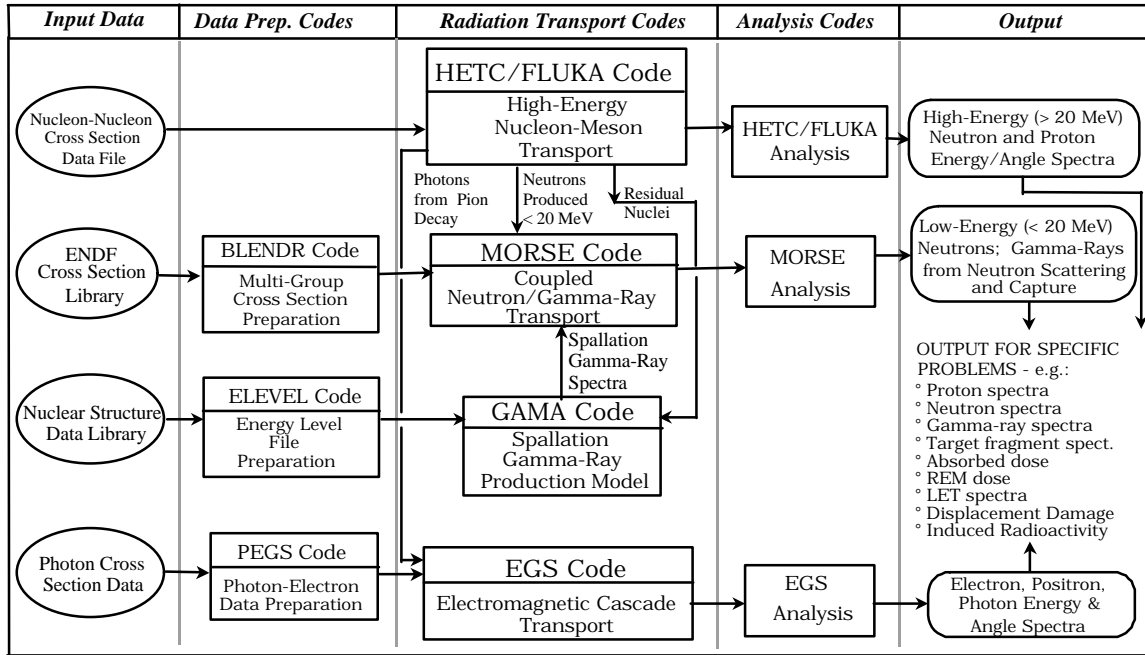To calculate the hadronic cascade contribution to the prompt background due to incident GCR protons, the FLUKA code [11] was used above 10 GeV, the HETC code [12] was used below 3 GeV, and a linear weighting of FLUKA and HETC secondary particle production from spallation collisions was used in the 3 - 10 GeV transition energy region. Neutrons below 20 MeV were transport using the MORSE code [13] with cross sections from the ENDF-V evaluated nuclear data base [14]. The electromagnetic cascade initiated by neutral pion decay was calculated using the EGS4 code [15].

2.4 Activation

The delayed background from induced radioactivity emissions caused by material activation was calculated using the procedure outlined in Fig. 4. Radioisotopes from spallation collisions produced by charged pions and by nucleons above 20 MeV were calculated using the intranuclear-cascade-evaporation nuclear interaction model contained in the HETC code. For the activation produced by low-energy (n,x) and (p,x) reactions, cross sections from the ENDF-V and BNL data bases [16] are normally used. In the present calculations, simplifying approximations were made: low-energy (p,x) production was neglected, and activation from low-
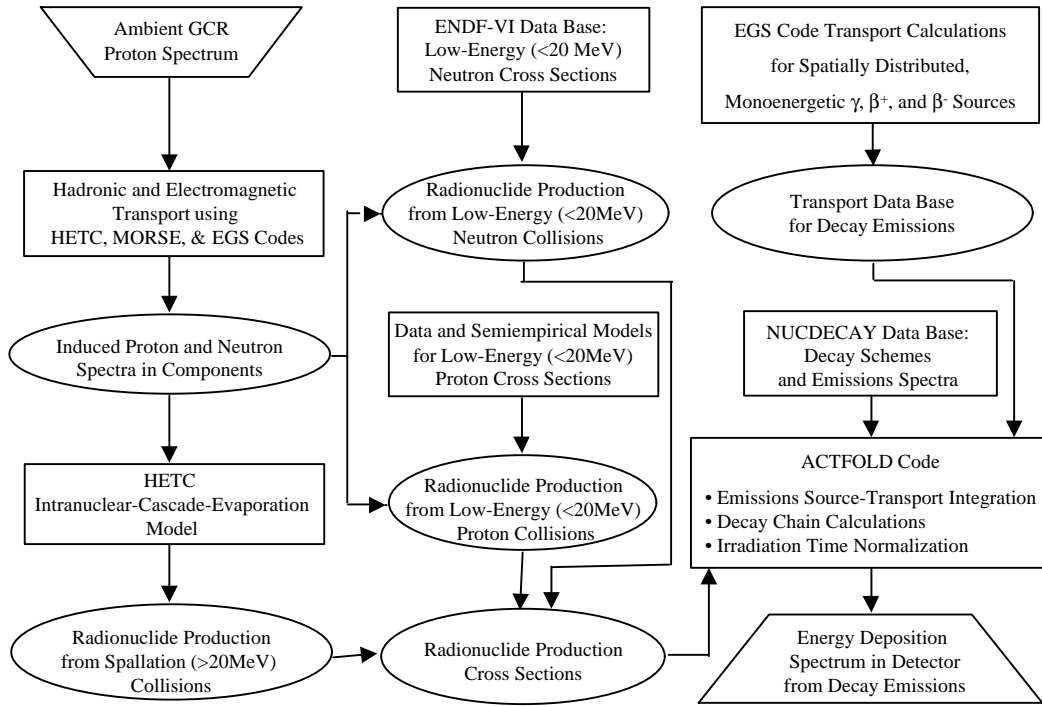
Fig. 4. Calculational procedure used for predicting activation backgrounds.

energy (n,x) reactions were included only for albedo neutron reactions with cadmium, as described later in Sec. 3.2.

The NUCDECAY data library [17] was used in determining nuclear decay emissions. The intensity and energy of individual decay particles (positrons, electrons, x-rays, or gamma-rays) were determined using Monte Carlo selections from frequencies obtained from NUCDECAY data so that decay mode correlations in producing energy deposition in the detector could be properly accounted for. The contributions of daughter and granddaughter radioisotopes were included by analytical decay chain calculations. Decay emissions were transported using the EGS4 code.

2.5 Analysis Assumptions

Anticoincidence counting restrictions were applied in registering background count rates from analyses of the Monte Carlo particle tracking and energy deposition calculations. Prompt background counts were rejected if particles from a source proton (or a diffuse x-ray) produced energy deposition above a threshold level in the BGO, and activation counts were vetoed if

energy deposition from a single radionuclide decay exceeded the BGO threshold. The BGO threshold was taken to be 100 keV.

In computing energy deposition in the BGO, the nonlinearity of light yield with energy deposition which occurs for densely ionizing particles (mainly alphas and recoil residual nuclei from nuclear interactions) was taken into account using Birk's formulation with a saturation parameter value of kB = 8.1 mg/MeV-cm^2 from [18].

Activation backgrounds were calculated at the end of a one year irradiation period.

3. RESULTS

3.1 L2 Orbit Background

Fig. 5 shows the background spectrum with component contributions for the L2 orbit. As indicated, the diffuse x-ray background dominates below 20 keV, and the BGO activation
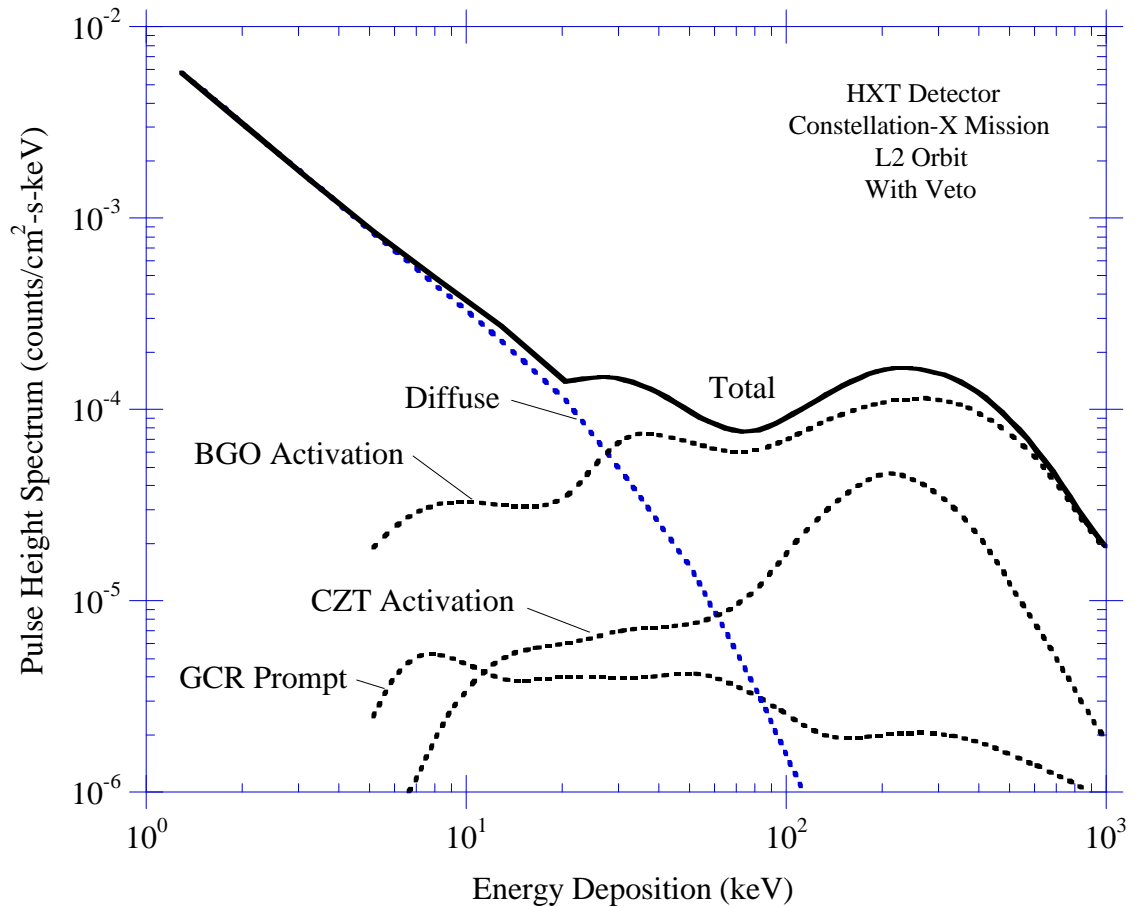

Fig. 5. Predicted HXT background spectra for L2 orbit.

background dominates at higher energies, giving a roughly constant count rate from 20 keV to several hundred keV of $\approx 10^{-4}$ cts/cm^2 - s - keV.

A tabulation of these results integrated over various energy intervals is given in Table 2 together with the "veto %" from anticoincidence counting based on energy deposition in the BGO above the rejection threshold of 100 keV. The contribution of background components for these energy ranges is shown in Table 3.

Table 2. Background count rates for L2 orbit.

		counts/s		counts/cm^2-s		
Component	E Range	no veto	with veto	no veto	with veto	veto %
GCR Prompt	5 - 20 keV	3.47E-03	3.95E-04	5.41E-04	6.16E-05	89%
	20 - 50 keV	8.74E-03	7.65E-04	1.36E-03	1.19E-04	91%
	50 - 100 keV	1.32E-02	1.06E-03	2.05E-03	1.65E-04	92%
	5 - 100 keV	2.54E-02	2.22E-03	3.95E-03	3.46E-04	91%
Diffuse	5 - 20 keV	2.75E-02	2.75E-02	4.28E-03	4.28E-03	0%
	20 - 50 keV	7.91E-03	7.91E-03	1.23E-03	1.23E-03	0%
	50 - 100 keV	1.71E-03	1.71E-03	2.67E-04	2.67E-04	0%
	5 - 100 keV	3.71E-02	3.71E-02	5.78E-03	5.78E-03	0%
BGO Activation	5 - 20 keV	9.99E-02	2.66E-03	1.56E-02	4.14E-04	97%
	20 - 50 keV	1.68E-01	1.36E-02	2.61E-02	2.12E-03	92%
	50 - 100 keV	1.87E-01	1.67E-02	2.91E-02	2.60E-03	91%
	5 - 100 keV	4.55E-01	3.30E-02	7.08E-02	5.14E-03	93%
CZT Activation	5 - 20 keV	4.68E-04	4.18E-04	7.30E-05	6.51E-05	11%
	20 - 50 keV	1.44E-03	1.34E-03	2.25E-04	2.08E-04	7%
	50 - 100 keV	2.71E-03	2.51E-03	4.21E-04	3.91E-04	7%
	5 - 100 keV	4.62E-03	4.26E-03	7.19E-04	6.64E-04	8%
Total	5 - 20 keV	1.31E-01	3.09E-02	2.05E-02	4.82E-03	76%
	20 - 50 keV	1.86E-01	2.36E-02	2.89E-02	3.68E-03	87%
	50 - 100 keV	2.05E-01	2.20E-02	3.19E-02	3.42E-03	89%
	5 - 100 keV	5.22E-01	7.65E-02	8.13E-02	1.19E-02	85%

Table 3. Contribution of background components to count rates (with veto) in various energy ranges - L2 orbit.

	5 - 20 keV	20 - 50 keV	50 - 100 keV	5 - 100 keV
GCR Prompt	1%	3%	5%	3%
Diffuse	89%	33%	8%	48%
BGO Activation	9%	58%	76%	43%
CZT Activation	1%	6%	11%	6%

3.2 LEO Orbit Background

For the LEO background, we assume that measurements are not made during passage through the South Atlantic anomaly region, which produces essentially all of the trapped proton exposure, so a prompt trapped proton background component is not considered.

The prompt GCR component has large time-dependent fluctuations due to the large variation in the effectiveness of geomagnetic shielding during the orbit. This is illustrated in Fig. 6, which shows an example of the predicted GCR flux variation over a 24-hour orbit duration. However, the calculations show that the GCR prompt background component is so small relative to other background contributions that this time variation is unimportant. Thus, an orbit-average GCR prompt background was used.

The GCR prompt component for LEO was estimated by scaling the GCR prompt background for the L2 orbit. Detailed code results from the L2 GCR prompt background calculations show that the main contribution arises from the electromagnetic cascade induced in the spacecraft by the decay of neutral pions produced by the hadronic cascade. Therefore, we
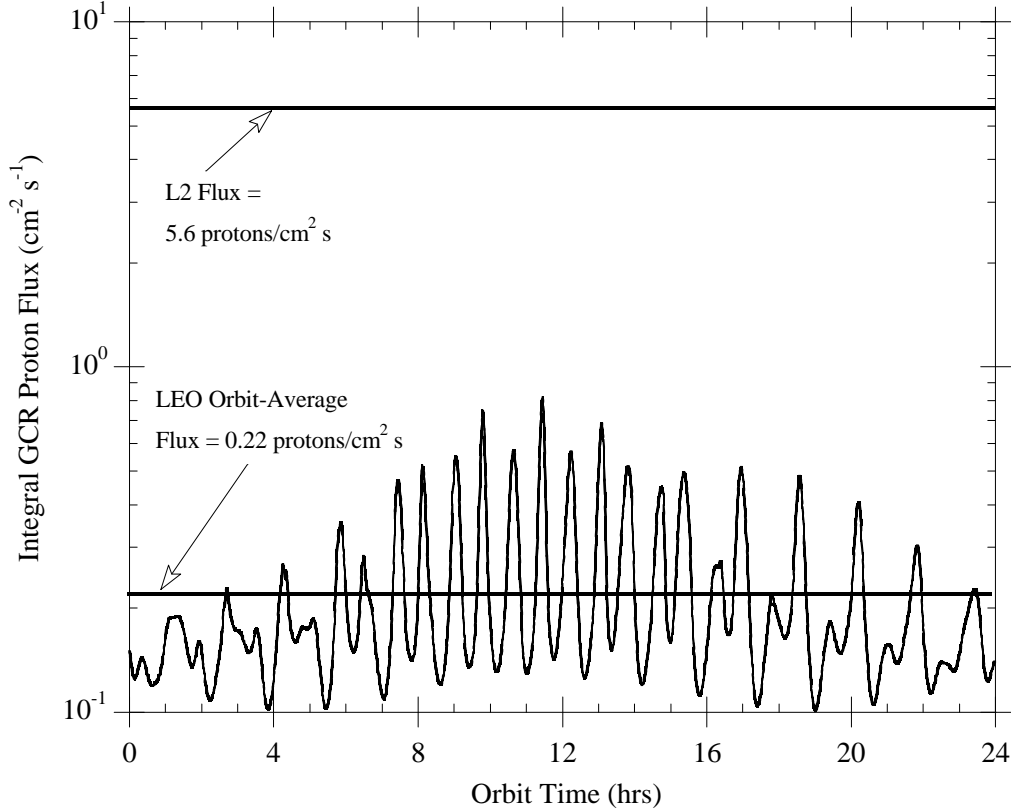

Fig. 6. Comparison of GCR proton flux for L2 and LEO (500 km, 28.5 deg) orbits.

used as a scaling factor the ratio of the GCR proton spectra for L2 and LEO (Fig. 2) integrated over the π^o production cross section. This results in a scaling factor of 14 – i.e., the LEO GCR prompt background is estimated to be a factor of 14 smaller than the L2 GCR prompt background. This is considered a more realistic scaling factor than if the GCR flux ratios neglecting spectral dependence were used, which, from values given in Fig. 6, would give a scaling factor of 5.6/0.22 = 25.

The LEO activation background cannot be scaled from the L2 background with acceptable accuracy. This is because the LEO activation is produced by trapped protons, not GCR protons as for the L2 orbit. The much softer trapped proton spectrum produces significantly different magnitudes for individual radionuclides and decay emissions compared to the hard GCR proton spectrum. Thus, for the LEO case additional activation calculations were performed using the trapped proton spectrum shown earlier in Fig. 2 as a source. The diffuse γ-ray background was taken to be the same for the LEO and L2 orbits.

The resulting LEO background estimate based on the above procedure is shown in Fig. 7. The results are qualitatively similar to the L2 orbit case in that the low-energy part of the spectrum, below about 20 keV, is dominated by the diffuse x-ray component with BGO activation dominating at higher energies. Quantitative comparisons of the LEO and L2 backgrounds are given below in Sec. 3.3 Tabulations of the LEO background count rates in various energy ranges and the fractional component contributions are given in Tables 4 and 5, respectively.

Activation spectra for the LEO orbit have been computed for a one year irradiation time, as was done for the L2 orbit activation. In general, the LEO activation can have short-term fluctuations due to the decay of short half-life radioisotopes after passage through the South Atlantic anomaly. However, in the present case the contribution of short half-life (< 20 min) radioisotopes is negligible, so the LEO activation increases monotonically with mission duration. Therefore, the one-year irradiation time comparisons for the L2 and LEO orbits are appropriate.

Since some isotopes of cadmium have relatively high neutron capture cross sections, we have also considered for the LEO activation the contribution to CZT activation produced by the neutron albedo environment. Using the predicted neutron albedo spectrum for a particular location (42° N geomagnetic latitude) from [19], the scaling methods described in [20] to obtain an orbit-average albedo neutron spectrum, and neutron cross sections from [16], we find that
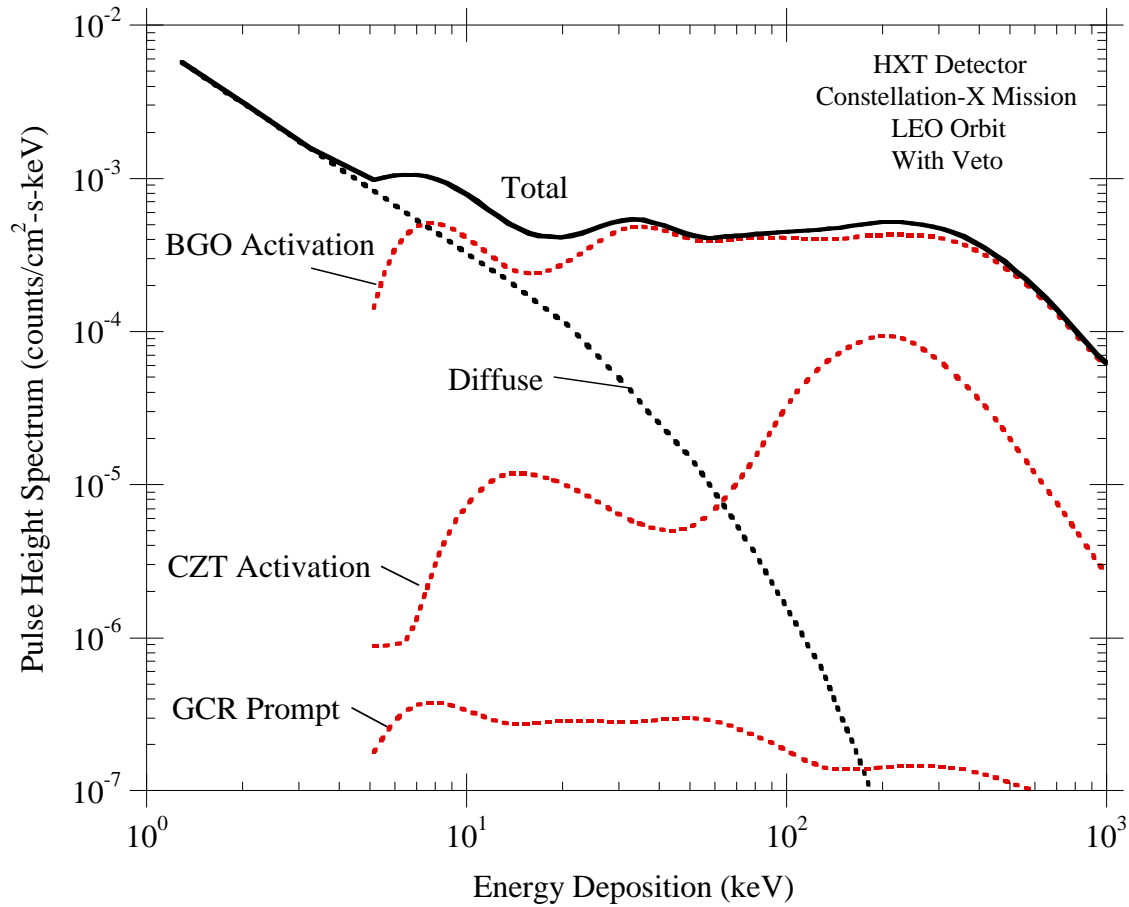
Fig. 7. Predicted HXT background spectra for LEO orbit.

activation from albedo neutron thermal and epithermal reactions in cadmium contained in the CZT detector amounts to about 8% of the CZT activation produced by trapped proton spallation interactions.

3.3 Comparison of Backgrounds for L2 and LEO Orbits

Background spectra for the L2 and LEO orbits are compared in Fig. 8 and Table 6. (The LEO activation background is expected to be an underestimate due to uncertainties in the trapped proton environment model. Comparisons of model predictions with activation measurements for a variety of materials aboard the LDEF satellite [21,22], which had an LEO orbit similar to that being considered here, indicate that the models used here underestimate the measured activation by about a factor of two.)

Table 4. Background HXT count rates for LEO orbit.

Component	E Range	counts/s		counts/cm^2-s		veto %
		no veto	with veto	no veto	with veto	
GCR Prompt	5 - 20 keV	2.48E-04	2.82E-05	3.87E-05	4.40E-06	89%
	20 - 50 keV	6.24E-04	5.46E-05	9.72E-05	8.51E-06	91%
	50 - 100 keV	9.40E-04	7.56E-05	1.46E-04	1.18E-05	92%
	5 - 100 keV	1.81E-03	1.58E-04	2.82E-04	2.47E-05	91%
Diffuse	5 - 20 keV	2.75E-02	2.75E-02	4.28E-03	4.28E-03	0%
	20 - 50 keV	7.91E-03	7.91E-03	1.23E-03	1.23E-03	0%
	50 - 100 keV	1.71E-03	1.71E-03	2.67E-04	2.67E-04	0%
	5 - 100 keV	3.71E-02	3.71E-02	5.78E-03	5.78E-03	0%
BGO Activation	5 - 20 keV	3.34E-01	2.86E-02	5.21E-02	4.45E-03	91%
	20 - 50 keV	5.41E-01	8.52E-02	8.43E-02	1.33E-02	84%
	50 - 100 keV	7.02E-01	1.28E-01	1.09E-01	1.99E-02	82%
	5 - 100 keV	1.58E+00	2.42E-01	2.46E-01	3.77E-02	85%
CZT Activation	5 - 20 keV	1.22E-03	9.03E-04	1.89E-04	1.41E-04	26%
	20 - 50 keV	1.60E-03	1.02E-03	2.50E-04	1.59E-04	36%
	50 - 100 keV	2.37E-03	1.46E-03	3.69E-04	2.27E-04	38%
	5 - 100 keV	5.19E-03	3.38E-03	8.08E-04	5.27E-04	35%
Total	5 - 20 keV	3.63E-01	5.70E-02	5.66E-02	8.88E-03	84%
	20 - 50 keV	5.51E-01	9.42E-02	8.58E-02	1.47E-02	83%
	50 - 100 keV	7.07E-01	1.31E-01	1.10E-01	2.04E-02	81%
	5 - 100 keV	1.62E+00	2.82E-01	2.53E-01	4.40E-02	83%

Table 5. Contribution of background components to count rates (with veto) in various
energy ranges - LEO orbit.

	5 - 20 keV	20 - 50 keV	50 - 100 keV	5 - 100 keV
GCR Prompt	0.05%	0.06%	0.06%	0.06%
Diffuse	48%	8%	1%	13%
BGO Activation	50%	90%	98%	86%
CZT Activation	1.6%	1.1%	1.1%	1.2%
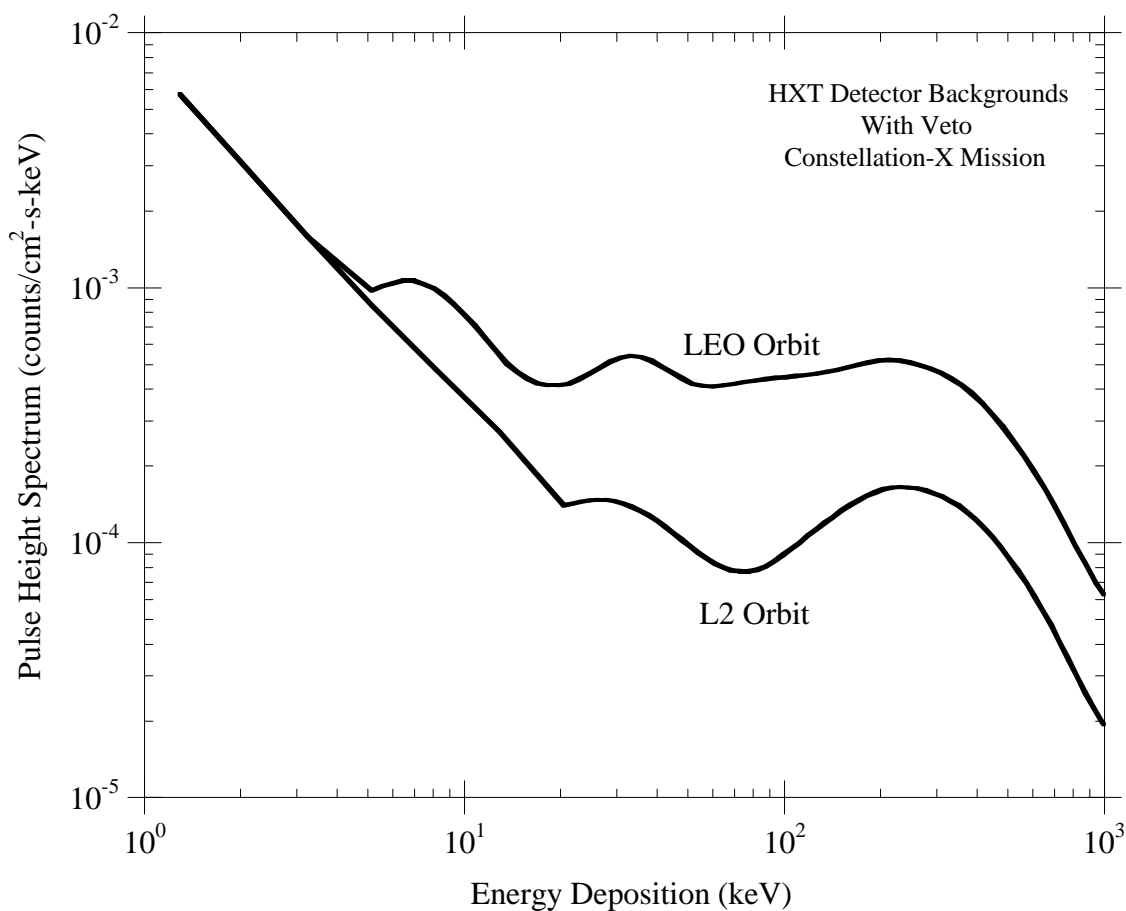
Fig. 8. Comparison of predicted HXT background spectra for L2 vs. LEO orbit.

Table 6. Ratio of background count rates (with veto) for LEO orbit (500 km x 500 km, 28.5°) compared to L2 orbit.

	5 - 20 keV	20 - 50 keV	50 - 100 keV	5 - 100 keV
GCR Prompt	0.071	0.071	0.071	0.071
Diffuse	1.0	1.0	1.0	1.0
BGO Activation	10.8	6.3	7.7	7.3
CZT Activation	2.2	0.8	0.6	0.8
All Components	1.8	4.0	6.0	3.7

The L2 vs. LEO background comparison indicates that the LEO background is substantially higher, by factors of 4 to 6 above 20 keV. The higher LEO background arises mainly because, for the particular detector assembly design considered, the dominant background component (above 20 keV, for both L2 and LEO) is BGO activation, and the orbit-average trapped proton flux which produces LEO activation is much higher (by a factor of 6) than the GCR proton flux which produces activation at L2.

It should be emphasized that the L2 vs. LEO backgrounds estimated here are expected to be strongly dependent on the particular detector design considered. For example, modifications to the present design that would reduce the BGO activation component (discussed in next section) would be expected to reduce the difference between the LEO and L2 total backgrounds.

4. CONCLUSIONS

Background estimates for a preliminary HXT hard x-ray detector design on Constellation-X spacecraft in an L2 orbit have been made for prompt GCR, activation, and diffuse x-ray background sources. The results show that, for the particular detector assembly design considered, the background at low energies (below about 20 keV) is dominated by the diffuse component and at higher energies from the activation of the BGO active shield and collimator. The x-ray background estimate for the baseline L2 orbit has been compared with the background expected for an alternative LEO orbit (taken to be 500 km x 500 km at 28.5° inclination), and it is found that the LEO background level in the high (> 20 keV) energy range is substantially higher (by about a factor of 5). However, this LEO vs. L2 background result is expected to be strongly dependent on detector assembly design, and could change significantly if the design is modified (as discussed below) for background reduction.

These background simulations suggest approaches for detector modifications that may provide significant background reduction. Two modifications are discussed below -- reduction of BGO thickness and using the BGO only as an active shield, not as a shield and collimator.

A difficulty of the detector design considered is that the BGO "overshields" the GCR-induced prompt component at the expense of providing a large BGO activation background component. Thus, the thickness of the BGO shield wall and bottom (currently 1.9 cm, or 13.5 g/cm^2) could be reduced to lower the BGO activation source volume. This would reduce the

veto efficiency somewhat and result in an increase of the GCR prompt background component, but, as indicated by Fig. 5, considerable increase would be acceptable. While the CZT activation would, in principle, increase if the BGO shielding is reduced, the material shielding effectiveness of the BGO is almost negligible for the hard GCR proton spectrum, so the CZT activation is not expected to increase appreciably if the BGO is made thinner.

Thus, simulations to quantify the decrease in BGO activation background, the increase in GCR prompt background, and the increase in CZT activation background as the BGO shield thickness is reduced would be useful to optimize the BGO shield for background reduction. The present simulations show that the GCR prompt contribution is dominated by interactions occurring in the spacecraft mass below the detector assembly (not interactions in the BGO), so the bottom thickness of the BGO should be considered separately from the wall thickness for an optimum shield. These results also suggest that a tapered BGO wall could be used to reduce weight.

The optimum BGO thickness for background reduction is expected to be different for the L2 and LEO orbits. This arises because the GCR proton flux is more than an order-of-magnitude lower in LEO than at L2, so the veto effectiveness requirement for the BGO is lower for LEO. Also, the material shielding effectiveness of the BGO in reducing CZT activation is different for the L2 and LEO ambient environments due to the large difference in the energy dependence of the trapped proton vs. GCR proton spectra.

For the simulations here using a thick-walled BGO shield and collimator, the high-energy detector background is dominated by BGO activation, not the CZT detector activation. However, if design modifications such as those discussed above are made which lead to a large reduction of the BGO activation component, then the CZT activation may become a significant contribution. Thus, CZT activation should not be generally dismissed as unimportant as the results presented here for the preliminary design might suggest.

The contributions of individual radioisotopes to the activation are given in the appendix.

REFERENCES

[1]   http://constellation.gsfc.nasa.gov/

[2]   F. Harrison (Caltech) and J. Tueller (NASA/GSFC), pri. comm. to B. Ramsey (1998).

[3]   O. Scheinman, NASA/GSFC, pri. comm. to T. Armstrong (1998).

[4]   G. D. Badhwar and D. M. O'Neill, "Improved Model of Galactic Cosmic Radiation for Space Exploration Missions", Nucl. Tracks & Radiat. Meas. 20 (3), 403 (1992).

[5]   Martin V. Zombeck, Handbook of Space Astronomy and Astrophysics, 2nd Edition, Cambridge University Press, Cambridge (1990).

[6]   Allan J. Tylka, et al., "CREME96: A Revision of the Cosmic Ray Effects on Micro-Electronics Code", IEEE Trans. Nucl. Sci. 44(6), 2150 (1997).

[7]   Donald M. Sawyer and James I. Vette, "AP-8 Trapped Proton Environment for Solar Maximum and Solar Minimum", National Science Data Center, Goddard Space Flight Center, NSSDC/WDC-A-R&S 76-06, 1976.

[8]   T. W. Armstrong and B. L. Colborn, "TRAP/SEE Code Users Manual for Predicting Trapped Radiation Environments", Science Applications International Corporation, Contractors Report for NASA/MSFC, SAIC-TN-99010, August 1999.

[9]   T. W. Armstrong, B. L. Colborn, K. L. Dietz, S.L. O'Dell, and M. C. Weisskopf, "AXAF Detector Backgrounds Produced by Cosmic Ray Protons", IEEE Conf. on High Energy Radiation Backgrounds in Space, ISBN 0-7803-4335-2 (1998).

[10]   T. W. Armstrong, B. L. Colborn, K. L. Dietz, and B. D. Ramsey, "Monte Carlo Simulations of Background Spectra in INTEGRAL Imager Detectors", to be published in Proc. 3rd INTEGRAL Workshop: The Extreme Universe, 14-18 Sept. 1998, Taorimina/Sicily, Italy.

[11]   P. A. Aarnio, A. Fasso, A. Ferrari, J. H. Mohring, J. Ranft, P. R. Sala, G. R. Stevenson, and J. M. Zazula, "FLUKA: Hadronic Benchmarks and Applications", in International Conference on Monte Carlo Simulation in High Energy and Nuclear Physics, Tallahassee, Florida, USA, 22-26 February 1993, Peter Dragvitsch, Stephan L. Linn, Mimi Burbank, Editors, World Scientific Publishing (1994).

[12]   T.W. Armstrong and B. L. Colborn, "A Thick-Target Radiation Transport Code for Low-Mass Heavy Ion Beams, HETC/LHI", Nucl. Instr. Meth. 169, 161 (1980).

[13]   E. A. Straker, W. H. Scott, and N. R. Byrn, "The MORSE Code with Combinatorial Geometry", Science Applications Report SAI-72-511-LJ (1972).

[14]   Evaluated Nuclear Data File ENDF/B-V, National Nuclear Data Center, Brookhaven National Laboratory, Upton, N.Y.

[15]   Walter R. Nelson, Hideo Hirayama, and David W. O. Rogers, "The EGS4 Code System", Stanford Linear Accelerator Center Report SLAC-265 (Dec. 1985).

[16]   National Nuclear Data Center, Brookhaven National Laboratory, Upton, N. Y. (http://www.nndc.bnl.gov/).

[17]   K. F. Eckerman, R. J. Westfall, J. C. Ryman, and M. Cristy, "Nuclear Decay Data Files of the Dosimetry Research Group", Oak Ridge National Laboratory, ORNL/TM-12350 (Dec. 1993).

[18]   P. R. Truscott, "Activation of Space-Borne Bismuth Germanate Gamma-Ray Detectors", Ph.D. Thesis, Univ. London (1996).

[19]   T.W. Armstrong, K. C. Chandler, and J. Barish, "Calculations of Neutron Flux Spectra Induced in the Earth's Atmosphere by Galactic Cosmic Rays", J. Geophy. Res., 2715 (1973).

[20]   T. W. Armstrong and B. L. Colborn, "Predictions of Secondary Neutron and Proton Fluxes Induced in the International Space Station by the Space Radiation Environment", Science Applications International Corporation, SAIC-TN-98042R (1998).

[21]   T. W. Armstrong, T. W. and B. L. Colborn, "Predictions of Induced Radioactivity for Spacecraft in Low Earth Orbit", Nucl. Tracks & Radiat. Meas. 20(1), 101 (1992).

[22]   T. W. Armstrong, B. L. Colborn, B. A. Harmon, and C. E. Laird, "Predictions of the Nuclear Activation of Materials on LDEF Produced by the Space Radiation Environment and Comparison with Flight Measurements", Radiat. Meas. 26(6), 765 (1996).

APPENDIX

Radioisotope Contributions to Activation Backgrounds

Some of the details of the activation background calculations showing the contributions of individual radioisotopes are given in this appendix. The most important radioisotopes are given both in terms of production magnitude and contribution to the background count rate, for both the CZT detector and BGO active collimator activation, and for both the L2 and LEO orbits.

A.1   Radiation Environment

The importance of particular radioisotopes is, of course, dependent on the radiation environments (proton and neutron flux spectra) associated with the specific orbit selections and detector assembly configuration considered. The ambient (or "external") and induced (or "internal") environments for the present calculations are shown in Figs. A-1 and A-2 for the L2 and LEO orbits, respectively. The volume-average proton (primary plus secondary protons) and secondary neutron spectra shown for the BGO collimator are also very good approximations for the spectra in the CZT detector. The spectra in the BGO from Figs. A-1 and A-2 are compared in Fig. A-3, which indicates that the main difference in radioisotope production composition for the two orbits is expected to be due to the much softer proton spectrum for LEO compared to L2. Table A-1 gives a summary of integral flux values.

A.2   Radioisotope Production

The magnitude of radioisotope production is given here in terms of the average production cross section, which is related to production by

$$P_i = [N_a / (<A> 1000)] (\Phi_p + \Phi_n) <\sigma_i>$$

where P_i is the specific production rate (g^{-1}-s^{-1}) for the ith-type radioisotope, N_a is Avogadro's constant, and $<A>$ is the average mass number of the material (110.2 for BGO, 101.8 for CZT). The factor 1000 converts the cross section from millibarn to barn units, and Φ_p and Φ_n are the integral proton and neutron fluxes, respectively, in the target material. The average production cross section (in millibarns) for the ith radioisotope product is defined as

$$< \sigma_i > \ = \ \frac{\int \phi_p(E) \, \sigma_i^p(E) \, dE \ \ + \ \ \int \phi_n(E) \, \sigma_i^n(E) \, dE}{\Phi_p + \Phi_n}$$

with $\Phi_p = \int \phi_p(E) dE$, $\Phi_n = \int \phi_n(E) dE$, and the differential flux spectra, $\phi_p(E)$ and $\phi_n(E)$, are from Fig. A-3.

Thus, $<\sigma_i>$ is an average over energy, neutron plus proton contribution, and all elements and natural isotopes of the target material (BGO or CZT, Table A-2). For spallation interactions, the energy limits are from 20 MeV to the maximum energies for the spectra (Fig. A-3). (For CZT production by neutrons < 20 MeV is also considered, as described later.)

Spallation production was calculated using the two-step intranuclear-cascade plus evaporation Monte Carlo nuclear model contained in the HETC code. The incident particle type (proton or neutron) was selected with probabilities based on the integral flux values (Table A-1), the energy of the incident particle was selected from the corresponding differential flux spectrum (Fig. A-3), and the target nucleus was selected based on the element and isotopic composition of the material (Table A-2). A Monte Carlo calculation for two-body interactions is then performed inside the target nucleus to determine the nucleon-pion cascade produced and particle emission. The residual energy following the intranuclear cascade is then used as input to a statistical (evaporation) model with Monte Carlo techniques to determine particle emission (p, n, d, t, He-3, or α) during nuclear de-excitation and the final A and Z of the residual nucleus. The results here are based on 100,000 incident particles for the Monte Carlo calculations.

Table A-3 gives the calculated spallation production cross sections for BGO ordered by element; Table A-4 gives the same values but ordered by cross section magnitude. The 76 radioisotopes listed are the major radioisotopes produced and are the ones used in the background calculations, but they are a subset of the total number produced. For the L2 orbit, a total of 1098 different isotopes were produced with 513 radioactive, and the 76 considered represent 80% of the total radioisotopes in terms of production cross section. For the LEO orbit, 370 stable plus radioactive isotopes are produced, 211 are radioactive, and the 76 considered represent 92% of the total radioisotopes in terms of production cross section.

Radioisotope production cross sections for the detector ordered by Z and A are given in Table A-5, and the same values ordered by magnitude are given in Table A-6. In this case a

time-saving approximation was made: the result of previous calculations made for the INTEGRAL solid state detector (ref. 20 of text) were scaled (by $\Phi_p + \Phi_n$ ratio) for use here. However, the INTEGRAL detector is CdTe, so the production from the Zn in the CdZnTe detector here is neglected in the results of Tables A-5 and A-6. This omission is not considered important to the overall background and conclusions here since for the particular detector assembly considered the BGO dominates the activation background.

In Tables A-5 and A-6 cross sections for ground and metastable (denoted by "m") states are listed separately. However, a shortcoming of the intranuclear-cascade-evaporation prediction method is that ground and metastable states cannot be distinguished. Therefore, in cases where metastable states are possible production modes, we have simply assigned one-half of the model-predicted production to the ground state and one-half to the metastable state. A few of the radioisotopes are listed with "a" or "b" suffixes to the mass number when neither isomer has been designated as a metastable state.

As an indication of the importance of radioisotopes produce by low-energy (< 20 MeV) neutrons, estimates for several low-energy reactions [(n,γ), (n, p), and (n, 2n)] were considered using cross section data from the literature (ref. 13 of text). These low-energy (< 20 MeV) production cross sections are compared spallation (> 20 MeV) cross sections in Table A-7. While the low-energy cross sections are larger than the spallation cross sections in several cases, they are always for cases where the combined cross sections are small, so the practical impact of the low-energy production is not significant. The only case where the low-energy reactions considered contribute appreciably is for Cd^{113m} production.

A-3   Radioisotope Contributions to Count Rate

Tables A-8 and A-9 give the contribution of individual radioisotopes to the detector count rate for the BGO collimator and detector activations, respectively, for one year irradiation times. The radioisotopes listed are the top 40 of the 90 different radioisotopes considered in the calculations; these 40 represent 90% or more of the total count rate. The count rate includes contributions over the entire range of energy depositions in the detector.

The radioisotope ranking in terms of count rate is somewhat different with veto (≥ 100 keV energy deposition in BGO) and without veto, so both cases are given in the tables. The contributions are listed by parent radioisotope; included under each parent are contributions from

the decay of any radioactive daughter and granddaughter products. On average, the daughter products contribute 30 – 45% to the total count rate for the different cases in Tables A-8 and A-9; granddaughter products typically contribute less than 5%.
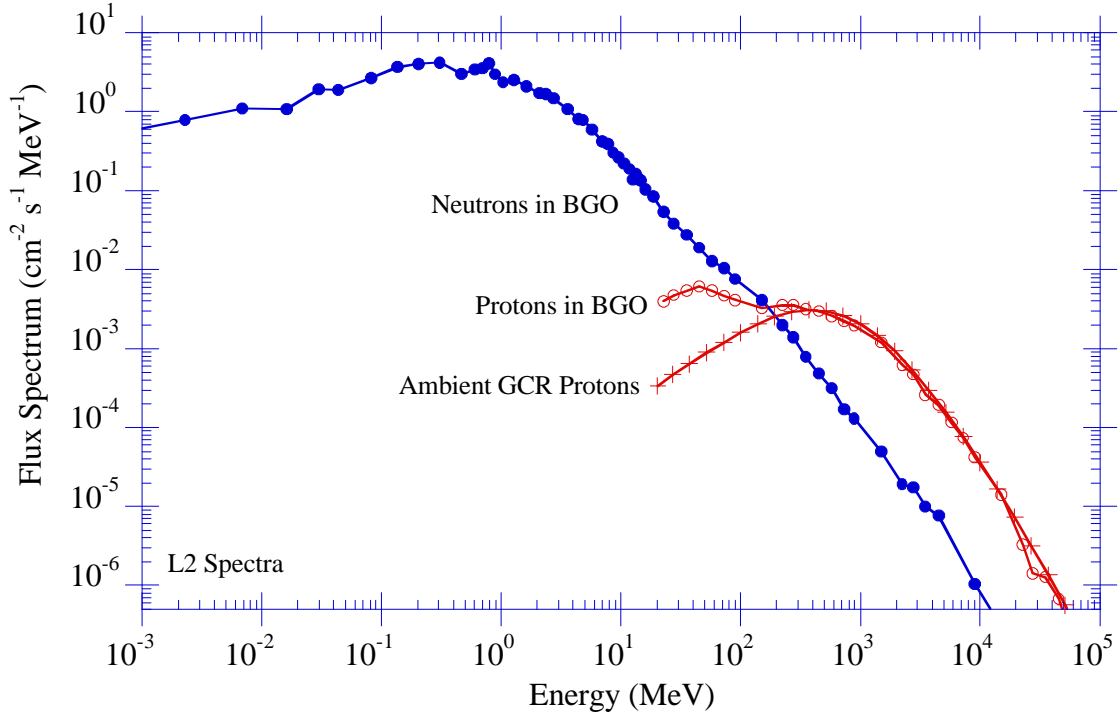
Fig. A-1.   Ambient proton spectrum (at solar minimum) and induced proton and
neutron spectra in BGO active collimator for L2 orbit.
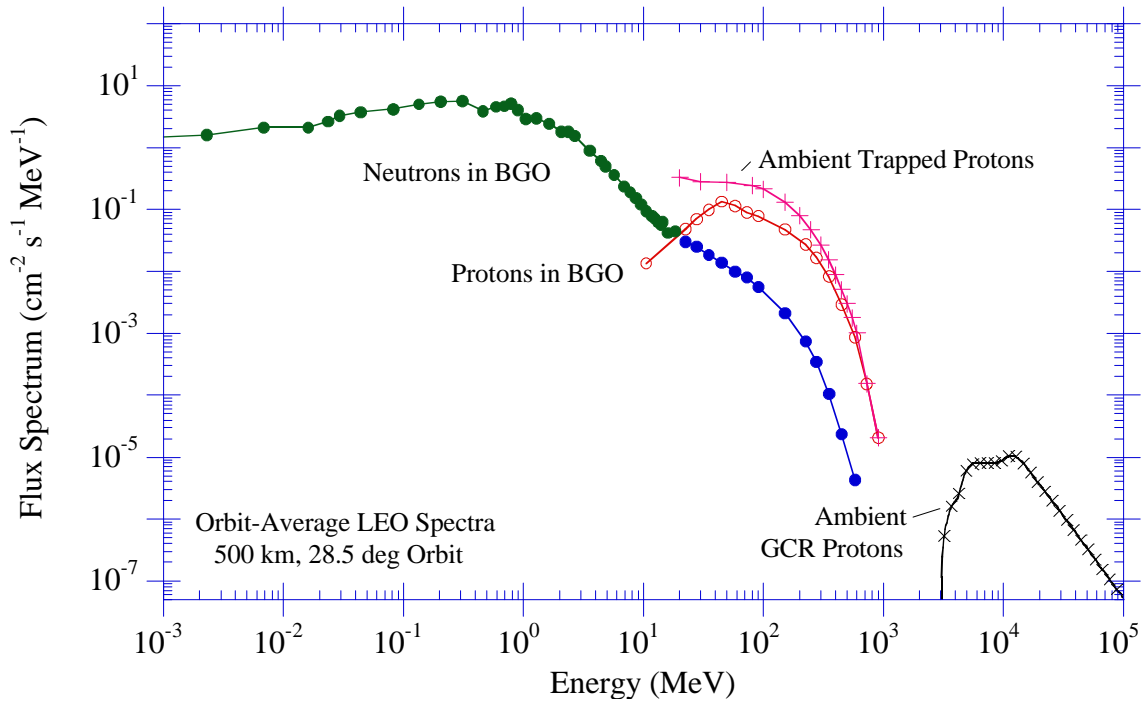
Fig. A-2. Ambient proton spectra (at solar minimum) and induced proton and neutron
spectra in BGO active collimator for LEO orbit.
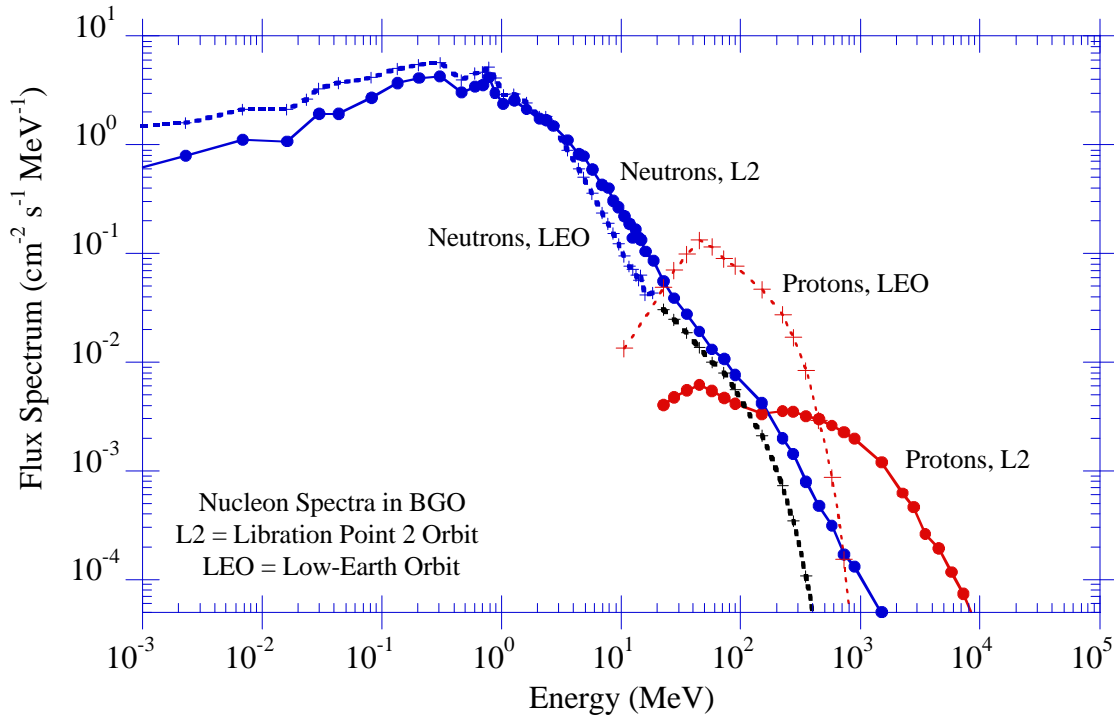
Fig. A-3. Comparison of nucleon spectra induced in BGO collimator for L2 and LEO orbits.

Table A-1. Ambient fluxes for L2 and LEO orbits (at solar minimum) and fluxes induced in BGO active collimator.

	Flux (cm^{-2} s^{-1})			
	Ambient		In BGO	
	L2 Orbit	LEO Orbit	L2 Orbit	LEO Orbit
GCR Protons > 20 MeV	5.6	0.22	5.7	0.22
Trapped Protons > 20 MeV	-	33	-	16
Neutrons > 20 MeV	-	0.15 (a)	2.2	1.3
Neutrons, all E	-	0.46 (a)	15	12

(a) Approximate estimate of albedo neutron flux

Table A-2. Natural isotopic compositions used for activation calculations.

Component	Material	Element	Isotope	Isotopic Fraction
Active Collimator	BGO	Bi	Bi-209	1
		Ge	Ge-70	0.205
			Ge-72	0.274
			Ge-73	0.078
			Ge-74	0.365
			Ge-76	0.078
		O	O-16	1
Detector	CZT	Cd	Cd-106	0.0125
			Cd-108	0.0089
			Cd-110	0.1251
			Cd-111	0.1281
			Cd-112	0.2413
			Cd-113	0.1222
			Cd-114	0.2872
			Cd-116	0.0747
		Zn	Zn-64	0.486
			Zn-66	0.279
			Zn-67	0.041
			Zn-68	0.188
		Te	Te-122	0.026
			Te-123	0.0091
			Te-124	0.0482
			Te-125	0.0718
			Te-126	0.1895
			Te-128	0.3169
			Te-130	0.338

Table A-3. Average radioisotope production cross sections for spallation interactions by neutrons and protons > 20 MeV in BGO active collimator.

| Element | Radioisotope | | Production Cross Section (mb) | | Ratio: |
	Z	A	L2 Orbit	LEO Orbit	LEO/L2
Po	84	209	1.68	7.59	4.51
Po	84	207	9.85	54.8	5.56
Po	84	205	6.19	47.8	7.72
Bi	83	207	41.8	39.3	0.94
Bi	83	206	36.0	34.3	0.95
Bi	83	205	22.5	26.7	1.18
Bi	83	204	15.2	20.6	1.36
Bi	83	203	4.46	6.62	1.48
Pb	82	205	6.79	3.84	0.57
Pb	82	204	6.21	4.58	0.74
Pb	82	203	5.24	4.85	0.93
Pb	82	202	4.19	13.4	3.20
Pb	82	201	4.76	23.5	4.92
Pb	82	200	4.44	20.2	4.54
Pb	82	199	3.28	12.6	3.83
Pb	82	198	2.55	7.52	2.95
Tl	81	202	2.53	1.99	0.79
Tl	81	201	7.35	10.2	1.39
Tl	81	200	9.80	14.0	1.42
Tl	81	199	8.97	14.2	1.59
Tl	81	198	8.05	11.1	1.38
Tl	81	197	6.23	9.37	1.51
Tl	81	195	3.35	3.91	1.17
Tl	81	194	2.23	1.96	0.88
Hg	80	199	3.78	2.36	0.63
Hg	80	197	4.41	5.89	1.34
Hg	80	195	4.24	6.60	1.56
Hg	80	194	4.63	7.25	1.57
Hg	80	193	4.63	7.08	1.53
Au	79	195	1.84	1.50	0.81
Au	79	194	2.53	2.35	0.93
Au	79	193	3.64	3.35	0.92
Pt	78	189	1.41	0.77	0.54
Pt	78	188	1.72	0.83	0.49
Pt	78	186	2.31	0.85	0.37
Ir	77	185	1.58	0.54	0.34
Ir	77	184	1.62	0.63	0.39
Ir	77	182	2.45	0.54	0.22

(continued)

Table A-3. (continued)

| Element | Radioisotope | | Production Cross Section (mb) | | Ratio: |
	Z	A	L2 Orbit	LEO Orbit	LEO/L2
Os	76	182	1.72	0.46	0.27
Os	76	181	2.18	0.53	0.24
Os	76	180	2.21	0.31	0.14
Ra	75	178	1.99	0.46	0.23
Ra	75	177	1.82	0.20	0.11
Ta	73	172	1.38	0.07	0.05
As	33	73	2.08	8.78	4.23
As	33	72	2.26	11.1	4.92
As	33	71	2.77	12.1	4.37
Ge	32	75	2.26	2.35	1.04
Ge	32	71	14.1	20.8	1.47
Ge	32	69	12.1	23.9	1.98
Ge	32	68	5.78	13.1	2.26
Ga	31	73	6.31	3.06	0.49
Ga	31	72	4.37	2.76	0.63
Ga	31	70	6.55	5.17	0.79
Ga	31	68	8.71	12.13	1.39
Ga	31	67	8.18	14.41	1.76
Ga	31	66	5.26	7.25	1.38
Zn	30	69	1.36	0.39	0.29
Zn	30	65	5.43	6.29	1.16
Zn	30	63	1.87	2.30	1.23
Cu	29	64	2.28	1.87	0.82
Cu	29	61	2.86	2.04	0.71
Ni	28	59	3.88	1.46	0.38
Co	27	58	2.16	0.63	0.29
Co	27	56	1.68	0.36	0.21
Fe	26	55	2.42	0.29	0.12
Mn	25	54	1.67	0.19	0.11
Mn	25	53	2.67	0.36	0.13
Mn	25	52	2.09	0.22	0.11
Cr	24	51	2.21	0.17	0.077
V	23	49	1.87	0.12	0.064
V	23	48	1.51	0.051	0.034
K	19	40	1.26	0.017	0.014
Cl	17	36	1.33	0.017	0.013
O	8	15	12.0	19.3	1.61
N	7	13	3.18	5.21	1.64

Table A-4. Like Table A-3 but sorted by cross section magnitude.

L2 Orbit				LEO Orbit			
	Radioisotope		Cross		Radioisotope		Cross
Element	Z	A	Section (mb)	Element	Z	A	Section (mb)
Bi	83	207	41.8	Po	84	207	54.8
Bi	83	206	36.0	Po	84	205	47.8
Bi	83	205	22.5	Bi	83	207	39.3
Bi	83	204	15.2	Bi	83	206	34.3
Ge	32	71	14.1	Bi	83	205	26.7
Ge	32	69	12.1	Ge	32	69	23.9
O	8	15	12.0	Pb	82	201	23.5
Po	84	207	9.85	Ge	32	71	20.8
Tl	81	200	9.80	Bi	83	204	20.6
Tl	81	199	8.97	Pb	82	200	20.2
Ga	31	68	8.71	O	8	15	19.3
Ga	31	67	8.18	Ga	31	67	14.4
Tl	81	198	8.05	Tl	81	199	14.2
Tl	81	201	7.35	Tl	81	200	14.0
Pb	82	205	6.79	Pb	82	202	13.4
Ga	31	70	6.55	Ge	32	68	13.1
Ga	31	73	6.31	Pb	82	199	12.6
Tl	81	197	6.23	Ga	31	68	12.1
Pb	82	204	6.21	As	33	71	12.1
Po	84	205	6.19	As	33	72	11.1
Ge	32	68	5.78	Tl	81	198	11.1
Zn	30	65	5.43	Tl	81	201	10.2
Ga	31	66	5.26	Tl	81	197	9.37
Pb	82	203	5.24	As	33	73	8.78
Pb	82	201	4.76	Po	84	209	7.59
Hg	80	194	4.63	Pb	82	198	7.52
Hg	80	193	4.63	Hg	80	194	7.25
Bi	83	203	4.46	Ga	31	66	7.25
Pb	82	200	4.44	Hg	80	193	7.08
Hg	80	197	4.41	Bi	83	203	6.62
Ga	31	72	4.37	Hg	80	195	6.60
Hg	80	195	4.24	Zn	30	65	6.29
Pb	82	202	4.19	Hg	80	197	5.89
Ni	28	59	3.88	N	7	13	5.21
Hg	80	199	3.78	Ga	31	70	5.17
Au	79	193	3.64	Pb	82	203	4.85
Tl	81	195	3.35	Pb	82	204	4.58
Pb	82	199	3.28	Tl	81	195	3.91

(continued)

Table A-4. (continued)

L2 Orbit				LEO Orbit			
Element	Radioisotope		Cross	Element	Radioisotope		Cross
	Z	A	Section (mb)		Z	A	Section (mb)
N	7	13	3.18	Pb	82	205	3.84
Cu	29	61	2.86	Au	79	193	3.35
As	33	71	2.77	Ga	31	73	3.06
Mn	25	53	2.67	Ga	31	72	2.76
Pb	82	198	2.55	Hg	80	199	2.36
Tl	81	202	2.53	Au	79	194	2.35
Au	79	194	2.53	Ge	32	75	2.35
Ir	77	182	2.45	Zn	30	63	2.30
Fe	26	55	2.42	Cu	29	61	2.04
Pt	78	186	2.31	Tl	81	202	1.99
Cu	29	64	2.28	Tl	81	194	1.96
As	33	72	2.26	Cu	29	64	1.87
Ge	32	75	2.26	Au	79	195	1.50
Tl	81	194	2.23	Ni	28	59	1.46
Os	76	180	2.21	Pt	78	186	0.85
Cr	24	51	2.21	Pt	78	188	0.83
Os	76	181	2.18	Pt	78	189	0.77
Co	27	58	2.16	Ir	77	184	0.63
Mn	25	52	2.09	Co	27	58	0.63
As	33	73	2.08	Ir	77	185	0.54
Ra	75	178	1.99	Ir	77	182	0.54
Zn	30	63	1.87	Os	76	181	0.53
V	23	49	1.87	Os	76	182	0.46
Au	79	195	1.84	Ra	75	178	0.46
Ra	75	177	1.82	Zn	30	69	0.39
Pt	78	188	1.72	Co	27	56	0.36
Os	76	182	1.72	Mn	25	53	0.36
Po	84	209	1.68	Os	76	180	0.31
Co	27	56	1.68	Fe	26	55	0.29
Mn	25	54	1.67	Mn	25	52	0.22
Ir	77	184	1.62	Ra	75	177	0.20
Ir	77	185	1.58	Mn	25	54	0.19
V	23	48	1.51	Cr	24	51	0.17
Pt	78	189	1.41	V	23	49	0.12
Ta	73	172	1.38	Ta	73	172	0.07
Zn	30	69	1.36	V	23	48	0.05
Cl	17	36	1.33	K	19	40	0.02
K	19	40	1.26	Cl	17	36	0.02

Table A-5. Average radioisotope production cross sections for spallation
interactions by neutrons and protons > 20 MeV in CdTe.

	Radioisotope		Production Cross Section (mb)		Ratio:
Element	Z	A	L2 Orbit	LEO Orbit	LEO/L2
I	53	128	1.90	14.0	7.37
I	53	126	3.52	24.8	7.05
I	53	125	3.82	26.4	6.92
I	53	124	3.51	25.7	7.31
I	53	123	3.18	19.7	6.20
I	53	122	2.68	14.5	5.40
Te	52	129	13.38	2.07	0.155
Te	52	129m	13.38	2.07	0.155
Te	52	127	19.92	10.8	0.54
Te	52	127m	19.92	10.8	0.54
Te	52	125m	17.76	11.1	0.62
Te	52	123	12.73	7.21	0.566
Te	52	123m	12.73	7.21	0.566
Te	52	121	5.89	7.21	1.23
Te	52	121m	5.89	7.21	1.23
Te	52	116	1.75	1.72	0.99
Sb	51	129	8.21	3.23	0.39
Sb	51	128a	2.73	0.791	0.289
Sb	51	128b	2.73	0.791	0.289
Sb	51	127	11.19	4.06	0.363
Sb	51	126	3.56	2.21	0.621
Sb	51	126m	3.56	2.21	0.621
Sb	51	125	10.46	4.43	0.423
Sb	51	124	2.96	1.10	0.370
Sb	51	124n	2.96	1.10	0.370
Sb	51	124m	2.96	1.10	0.370
Sb	51	122	6.79	3.44	0.507
Sb	51	120a	3.12	2.06	0.662
Sb	51	120b	3.12	2.06	0.662
Sb	51	119	6.05	4.50	0.743
Sb	51	118	2.66	2.10	0.788
Sb	51	118m	2.66	2.10	0.788
Sb	51	117	4.83	3.53	0.730
Sb	51	116	1.93	1.69	0.873
Sb	51	116m	1.93	1.69	0.873
Sb	51	115	2.95	1.97	0.666
Sn	50	113	3.31	1.92	0.579
Sn	50	111	2.22	0.931	0.420

(continued)

Table A-5. (continued)

Element	Radioisotope Z	A	Production Cross Section (mb) L2 Orbit	LEO Orbit	Ratio: LEO/L2
In	49	112	4.98	15.9	3.19
In	49	111	3.12	11.2	3.59
In	49	111m	3.12	11.2	3.59
In	49	110a	3.24	12.9	3.98
In	49	110b	3.24	12.9	3.98
In	49	109	6.20	25.2	4.06
Cd	48	113	16.2	5.98	0.369
Cd	48	113m	16.2	5.98	0.369
Cd	48	109	42.7	22.6	0.529
Cd	48	107	19.3	15.4	0.799
Cd	48	104	4.87	5.53	1.14
Ag	47	112	9.11	2.27	0.249
Ag	47	111	14.8	4.29	0.290
Ag	47	110	6.37	2.17	0.341
Ag	47	110m	6.37	2.17	0.341
Ag	47	109m	6.84	2.34	0.341
Ag	47	108	5.33	2.11	0.396
Ag	47	108m	5.33	2.11	0.396
Ag	47	106	5.14	2.28	0.444
Ag	47	106m	5.14	2.28	0.444
Ag	47	105	9.05	4.92	0.543
Ag	47	104	4.52	2.52	0.558
Ag	47	104m	4.52	2.52	0.558
Ag	47	103	6.65	4.11	0.618
Ag	47	102	4.75	3.83	0.806
Pd	46	103	3.63	1.44	0.397
Pd	46	101	4.86	2.74	0.564
Pd	46	100	5.57	3.87	0.694
Rh	45	100	3.64	1.35	0.371
Rh	45	99	2.66	1.05	0.397
Rh	45	99m	2.66	1.05	0.397
Ru	44	97	3.06	0.703	0.229
Nb	41	90	3.94	0.984	0.250
Zr	40	89	3.20	0.387	0.121
Zr	40	88	2.07	0.422	0.204
Y	39	88	1.60	0.123	0.0767
Y	39	87	1.78	0.193	0.108
Rb	37	80	1.99	0.088	0.0440
Kr	36	79	2.72	0.105	0.0387

(continued)

Table A-5. (continued)

| Element | Radioisotope | | Production Cross Section (mb) | | Ratio: |
	Z	A	L2 Orbit	LEO Orbit	LEO/L2
Kr	36	77	1.69	0.0351	0.02074
Br	35	77	2.06	0.0703	0.03416
Br	35	76	2.31	0.0878	0.03806
Se	34	75	1.79	1.00E-04	5.58E-05
As	33	72	1.78	0.035	0.020
As	33	71	1.71	0.0527	0.03078
Ge	32	69	2.02	0.0088	0.00435
Ga	31	68	2.08	0.018	0.00843
Ga	31	67	2.42	1.00E-05	4.13E-06
Zn	30	65	1.84	17.5	9.50
Cu	29	62	2.05	33.6	16.4
Co	27	57	1.74	4.74	2.73
Mn	25	53	1.62	2.85	1.76

Table A-6. Like Table A-5 but sorted by cross section magnitude.

L2 Orbit				LEO Orbit			
	Radioisotope		Cross		Radioisotope		Cross
Element	Z	A	Section (mb)	Element	Z	A	Section (mb)
Cd	48	109	42.7	Cu	29	62	33.6
Te	52	127	19.9	I	53	125	26.4
Te	52	127m	19.9	I	53	124	25.7
Cd	48	107	19.3	In	49	109	25.2
Te	52	125m	17.8	I	53	126	24.8
Cd	48	113	16.2	Cd	48	109	22.6
Cd	48	113m	16.2	I	53	123	19.7
Ag	47	111	14.8	Zn	30	65	17.5
Te	52	129	13.4	In	49	112	15.9
Te	52	129m	13.4	Cd	48	107	15.4
Te	52	123	12.7	I	53	122	14.5
Te	52	123m	12.7	I	53	128	14.0
Sb	51	127	11.2	In	49	110a	12.9
Sb	51	125	10.5	In	49	110b	12.9
Ag	47	112	9.11	In	49	111	11.2
Ag	47	105	9.05	In	49	111m	11.2
Sb	51	129	8.21	Te	52	125m	11.1
Ag	47	109m	6.84	Te	52	127	10.8
Sb	51	122	6.79	Te	52	127m	10.8
Ag	47	103	6.65	Te	52	123	7.21
Ag	47	110	6.37	Te	52	123m	7.21
Ag	47	110m	6.37	Te	52	121	7.21
In	49	109	6.20	Te	52	121m	7.21
Sb	51	119	6.05	Cd	48	113	5.98
Te	52	121	5.89	Cd	48	113m	5.98
Te	52	121m	5.89	Cd	48	104	5.53
Pd	46	100	5.57	Ag	47	105	4.92
Ag	47	108	5.33	Co	27	57	4.74
Ag	47	108m	5.33	Sb	51	119	4.50
Ag	47	106	5.14	Sb	51	125	4.43
Ag	47	106m	5.14	Ag	47	111	4.29
In	49	112	4.98	Ag	47	103	4.11
Cd	48	104	4.87	Sb	51	127	4.06
Pd	46	101	4.86	Pd	46	100	3.87
Sb	51	117	4.83	Ag	47	102	3.83
Ag	47	102	4.75	Sb	51	117	3.53
Ag	47	104	4.52	Sb	51	122	3.44
Ag	47	104m	4.52	Sb	51	129	3.23

(continued)

Table A-6. (continued)

L2 Orbit			LEO Orbit		
	Radioisotope	Cross		Radioisotope	Cross
Element	Z	A	Section (mb)	Element	Z	A	Section (mb)
Nb	41	90	3.94	Mn	25	53	2.85
I	53	125	3.82	Pd	46	101	2.74
Rh	45	100	3.64	Ag	47	104	2.52
Pd	46	103	3.63	Ag	47	104m	2.52
Sb	51	126	3.56	Ag	47	109m	2.34
Sb	51	126m	3.56	Ag	47	106	2.28
I	53	126	3.52	Ag	47	106m	2.28
I	53	124	3.51	Ag	47	112	2.27
Sn	50	113	3.31	Sb	51	126	2.21
In	49	110a	3.24	Sb	51	126m	2.21
In	49	110b	3.24	Ag	47	110	2.17
Zr	40	89	3.20	Ag	47	110m	2.17
I	53	123	3.18	Ag	47	108	2.11
Sb	51	120a	3.12	Ag	47	108m	2.11
Sb	51	120b	3.12	Sb	51	118	2.10
In	49	111	3.12	Sb	51	118m	2.10
In	49	111m	3.12	Te	52	129	2.07
Ru	44	97	3.06	Te	52	129m	2.07
Sb	51	124	2.96	Sb	51	120a	2.06
Sb	51	124n	2.96	Sb	51	120b	2.06
Sb	51	124m	2.96	Sb	51	115	1.97
Sb	51	115	2.95	Sn	50	113	1.92
Sb	51	128a	2.73	Te	52	116	1.72
Sb	51	128b	2.73	Sb	51	116	1.69
Kr	36	79	2.72	Sb	51	116m	1.69
I	53	122	2.68	Pd	46	103	1.44
Sb	51	118	2.66	Rh	45	100	1.35
Sb	51	118m	2.66	Sb	51	124	1.10
Rh	45	99	2.66	Sb	51	124n	1.10
Rh	45	99m	2.66	Sb	51	124m	1.10
Ga	31	67	2.42	Rh	45	99	1.05
Br	35	76	2.31	Rh	45	99m	1.05
Sn	50	111	2.22	Nb	41	90	0.984
Ga	31	68	2.08	Sn	50	111	0.931
Zr	40	88	2.07	Sb	51	128a	0.791
Br	35	77	2.06	Sb	51	128b	0.791
Cu	29	62	2.05	Ru	44	97	0.703
Ge	32	69	2.02	Zr	40	88	0.422

(continued)

Table A-6. (continued)

L2 Orbit				LEO Orbit			
	Radioisotope		Cross		Radioisotope		Cross
Element	Z	A	Section (mb)	Element	Z	A	Section (mb)
Rb	37	80	1.99	Zr	40	89	0.387
Sb	51	116	1.93	Y	39	87	0.193
Sb	51	116m	1.93	Y	39	88	0.123
I	53	128	1.90	Kr	36	79	0.105
Zn	30	65	1.84	Rb	37	80	0.088
Se	34	75	1.79	Br	35	76	0.0878
Y	39	87	1.78	Br	35	77	0.0703
As	33	72	1.78	As	33	71	0.0527
Te	52	116	1.75	Kr	36	77	0.0351
Co	27	57	1.74	As	33	72	0.0351
As	33	71	1.71	Ga	31	68	0.0176
Kr	36	77	1.69	Ge	32	69	8.78E-03
Mn	25	53	1.62	Se	34	75	1.00E-04
Y	39	88	1.60	Ga	31	67	1.00E-05

Table A-7. Spallation vs. low-energy neutron radioisotope production for CdTe.

| Radioisotope | | | Cross Section (mb) | | | |
| | | | L2 Orbit | | LEO Orbit | |
Element	Z	A	Spallation	Low-E Neutrons	Spallation	Low-E Neutrons
Cd	48	117	0.043	0.23	0.0088	0.19
Cd	48	117m	0.043	0.10	0.0088	0.082
Cd	48	115	0.077	4.7	0.0093	4.0
Cd	48	115m	0.077	3.56	0.0093	3.0
Cd	48	113m	16	11	6.0	8.8
Cd	48	111m	26	4.2	11	3.5
Cd	48	109	43	4.0	23	3.3
Cd	48	107	19	0.45	15	0.38
Cd	48	105	11	0.30	11	0.25
Ag	47	116	0.0	0.090	0.0	0.075
Ag	47	114	0.0	0.28	0.061	0.23
Ag	47	114m	0.0	0.26	0.061	0.22
Ag	47	112	9.1	0.82	2.3	0.68
Ag	47	111	15	0.28	4.3	0.23
Ag	47	110	6.4	0.35	2.2	0.29
Ag	47	110m	6.4	0.28	2.2	0.23
Ag	47	108	5.3	0.049	2.1	0.041
Ag	47	108m	5.3	0.045	2.1	0.038
Ag	47	106	5.1	0.14	2.3	0.11
Ag	47	106m	5.1	0.049	2.3	0.041

Table A-8. Contribution of radioisotopes produced in BGO to detector count rate.

L2 Orbit				LEO Orbit			
Without Veto		With Veto		Without Veto		With Veto	
Parent Isotope	Counts/s	Parent Isotope	Counts/s	Parent Isotope	Counts/s	Parent Isotope	Counts/s
Po-205	2.93E-01	Po-205	5.04E-02	Po-205	2.31E+00	Po-205	3.88E-01
Bi-206	2.53E-01	Bi-206	4.95E-02	Po-207	9.86E-01	Po-207	1.71E-01
Bi-204	2.11E-01	Bi-204	4.00E-02	Pb-200	8.10E-01	Pb-200	1.62E-01
Bi-205	1.84E-01	Bi-205	3.23E-02	Pb-199	6.15E-01	Pb-201	1.39E-01
Pb-200	1.45E-01	Pb-200	2.62E-02	Bi-204	6.13E-01	Pb-199	1.34E-01
Pb-198	1.32E-01	Pb-199	2.47E-02	Ge-69	5.45E-01	Bi-204	1.14E-01
Ge-69	1.26E-01	Tl-195	2.35E-02	Pb-198	5.29E-01	Bi-206	1.03E-01
Pb-199	1.06E-01	Tl-197	1.95E-02	Bi-206	5.23E-01	Bi-205	8.33E-02
Tl-198	9.33E-02	Pb-201	1.78E-02	Pb-201	4.84E-01	Pb-198	7.14E-02
Tl-200	9.19E-02	Hg-193	1.78E-02	Bi-205	4.74E-01	Tl-195	6.63E-02
Po-207	8.51E-02	Pb-198	1.64E-02	As-72	3.18E-01	Tl-197	6.22E-02
Ge-68	7.72E-02	Bi-203	1.57E-02	Tl-200	2.85E-01	Ge-69	5.56E-02
Tl-195	7.65E-02	Po-207	1.48E-02	Tl-198	2.80E-01	Hg-193	5.16E-02
Tl-197	7.14E-02	Tl-199	1.46E-02	Ge-68	2.75E-01	Tl-199	5.04E-02
Ga-66	7.01E-02	Tl-200	1.43E-02	As-71	2.64E-01	Bi-203	4.50E-02
Ir-182	6.73E-02	Ir-182	1.38E-02	Tl-197	2.32E-01	Tl-200	4.42E-02
Bi-203	6.67E-02	Ge-69	1.30E-02	Tl-195	2.13E-01	Hg-195	3.38E-02
Ga-68	5.53E-02	Hg-195	1.07E-02	Ga-66	2.10E-01	Ga-67	3.04E-02
Tl-199	5.49E-02	Tl-198	9.99E-03	Bi-203	2.03E-01	Tl-198	3.00E-02
Ga-72	5.44E-02	Os-181	8.51E-03	Tl-199	1.90E-01	As-71	2.82E-02
Hg-193	5.19E-02	Tl-194	8.34E-03	Ga-68	1.67E-01	As-72	2.34E-02
Tl-194	5.11E-02	Re-177	7.98E-03	Hg-193	1.50E-01	Tl-201	2.06E-02
Pb-201	5.02E-02	Ga-67	7.96E-03	Ga-67	1.05E-01	Ge-68	2.03E-02
Os-181	3.85E-02	Tl-201	6.84E-03	Tl-194	1.00E-01	Tl-194	1.64E-02
Re-177	3.39E-02	Re-178	6.09E-03	Hg-195	8.36E-02	Ga-66	1.55E-02
Re-178	3.07E-02	Au-193	5.64E-03	Ga-72	7.48E-02	Hg-197	1.27E-02
As-72	2.96E-02	Ge-68	5.63E-03	Zn-63	6.62E-02	Ga-68	1.15E-02
As-71	2.86E-02	Ga-66	5.20E-03	Hg-194	4.75E-02	Au-193	1.14E-02
Cu-61	2.75E-02	Os-182	4.69E-03	Au-194	4.72E-02	Pb-203	9.01E-03
Ga-67	2.74E-02	Ta-172	4.65E-03	Ga-70	4.32E-02	Ir-182	7.44E-03
Hg-195	2.55E-02	Pb-203	4.50E-03	Cu-61	4.27E-02	Hg-194	6.50E-03
Ga-70	2.52E-02	Hg-197	4.37E-03	Ir-182	3.58E-02	Au-194	6.45E-03
Ta-172	2.51E-02	Ga-72	4.24E-03	Au-193	3.45E-02	Ga-72	5.82E-03
Zn-63	2.48E-02	Os-180	4.10E-03	Zn-65	2.74E-02	As-73	5.07E-03
Hg-194	2.34E-02	Ir-185	4.09E-03	Pt-188	2.58E-02	Pt-189	4.98E-03
Au-194	2.33E-02	Pt-188	4.09E-03	Pt-186	2.53E-02	Os-181	4.93E-03
Pt-188	2.10E-02	Pt-189	3.96E-03	Ge-75	2.43E-02	Pb-204m	4.76E-03
Pt-186	2.09E-02	As-71	3.83E-03	Os-181	2.19E-02	Pt-188	4.72E-03
Ir-184	1.92E-02	Ga-68	3.82E-03	Tl-201	2.15E-02	Ge-71	4.38E-03
Ga-73	1.91E-02	Ga-73	3.23E-03	Pb-203	2.03E-02	Ga-70	4.36E-03
Total:	2.91		0.54		11.5		2.06

Table A-9. Contribution of radioisotopes produced in detector to detector count rate.

L2 Orbit				LEO Orbit			
Without Veto		With Veto		Without Veto		With Veto	
Parent Isotope	Counts/s	Parent Isotope	Counts/s	Parent Isotope	Counts/s	Parent Isotope	Counts/s
Te-127m	9.56E-03	Te-127m	8.90E-03	In-109	1.70E-02	In-109	1.29E-02
Sb-127	7.28E-03	Sb-127	6.65E-03	In-111m	1.23E-02	In-111m	1.22E-02
Te-129m	6.99E-03	Te-129m	6.36E-03	Te-127m	1.13E-02	Te-127m	1.05E-02
Sb-129	5.22E-03	Sb-129	4.67E-03	I-124	9.67E-03	I-125	9.51E-03
In-109	4.55E-03	In-109	4.09E-03	I-125	9.51E-03	I-126	7.50E-03
Sb-125	3.65E-03	Sb-125	3.55E-03	I-126	9.42E-03	Te-121m	6.67E-03
Te-127	3.41E-03	Te-127	3.12E-03	I-123	7.22E-03	Sb-127	6.48E-03
Cd-107	3.30E-03	Cd-109	3.03E-03	Sb-127	7.10E-03	I-123	6.48E-03
Cd-109	3.03E-03	Te-125m	2.89E-03	Te-121m	6.88E-03	I-124	5.26E-03
Ag-103	2.97E-03	Te-121m	2.50E-03	In-112	5.92E-03	Sn-111	4.70E-03
Te-125m	2.95E-03	Cd-107	2.50E-03	Cd-107	5.73E-03	Sb-125	4.54E-03
Pd-100	2.62E-03	Ag-111	2.36E-03	Cu-62	5.70E-03	Cd-107	4.34E-03
Te-121m	2.58E-03	Ag-110m	2.23E-03	I-122	5.58E-03	I-128	4.27E-03
Ag-110m	2.55E-03	Ag-103	2.17E-03	I-128	5.46E-03	In-112	4.25E-03
Ag-111	2.50E-03	Te-129	2.14E-03	Cd-104	5.13E-03	In-111	4.08E-03
Cd-104	2.48E-03	Te-123m	1.88E-03	In-110a	4.85E-03	Te-125m	3.93E-03
Ag-104m	2.39E-03	Pd-100	1.73E-03	Sn-111	4.78E-03	Te-127	3.69E-03
Te-129	2.32E-03	Sb-126m	1.72E-03	In-110b	4.77E-03	In-110b	3.65E-03
Pd-101	1.92E-03	In-111m	1.56E-03	Sb-125	4.66E-03	Cd-109	3.49E-03
Te-123m	1.89E-03	Sb-124n	1.51E-03	In-111	4.10E-03	Sb-129	2.89E-03
Sb-126m	1.89E-03	Sb-124m	1.39E-03	Te-127	4.02E-03	In-110a	2.81E-03
Ag-112	1.64E-03	Pd-101	1.38E-03	Te-125m	4.02E-03	Cd-104	2.80E-03
Sb-124m	1.57E-03	Pd-103	1.35E-03	Ag-103	3.69E-03	Ag-103	2.62E-03
In-111m	1.57E-03	Cd-104	1.29E-03	Pd-100	3.50E-03	Sn-113	2.61E-03
Ag-105	1.55E-03	Sn-113	1.23E-03	Cd-109	3.49E-03	Te-121	2.60E-03
Sb-124n	1.55E-03	Sn-111	1.20E-03	Sb-129	3.27E-03	Pd-100	2.40E-03
Pd-103	1.38E-03	Ag-105	1.18E-03	Ag-104m	2.90E-03	Sb-126m	2.33E-03
Sn-111	1.27E-03	Ag-109m	1.15E-03	Te-121	2.66E-03	Te-123m	2.32E-03
Sn-113	1.25E-03	Sb-122	1.14E-03	Sn-113	2.65E-03	Te-129m	2.14E-03
Sb-122	1.19E-03	Sb-119	1.02E-03	Sb-126m	2.55E-03	Ag-110m	1.66E-03
Ag-109m	1.15E-03	Ag-110	9.92E-04	Te-129m	2.35E-03	Sb-119	1.65E-03
Ag-110	1.14E-03	Te-121	9.74E-04	Te-123m	2.33E-03	Pd-101	1.61E-03
Sb-119	1.02E-03	Ag-112	9.36E-04	Pd-101	2.27E-03	I-122	1.54E-03
Te-121	9.99E-04	Ag-104m	9.31E-04	Te-116	1.91E-03	Ag-111	1.49E-03
Kr-77	9.55E-04	Ag-106m	7.71E-04	Ag-110m	1.89E-03	Te-116	1.43E-03
Te-116	9.28E-04	Zr-88	7.70E-04	Ag-105	1.84E-03	Ag-105	1.40E-03
Ag-108m	9.26E-04	Te-116	6.93E-04	Sb-119	1.65E-03	Sb-122	1.25E-03
Ag-108	9.16E-04	Kr-77	6.93E-04	Ag-111	1.58E-03	Sb-124n	1.22E-03
Ag-106	8.82E-04	Y-87	6.72E-04	Ag-102	1.45E-03	Ag-104m	1.13E-03
Ag-106m	8.66E-04	As-71	6.68E-04	Sb-122	1.31E-03	Sb-124m	1.12E-03
Total:	0.099		0.086		0.20		0.16